catalysts

MDPI

Article

Ru–Pd Bimetallic Catalysts Supported on CeO_2-MnO_X Oxides as Efficient Systems for H_2 Purification through CO Preferential Oxidation

Roberto Fiorenza [1], Luca Spitaleri [1], Antonino Gulino [1,2] and Salvatore Scirè [1,*]

[1] Dipartimento di Scienze Chimiche, Università di Catania, Viale A. Doria 6, 95125 Catania, Italy; rfiorenza@unict.it (R.F.); lucaspitaleri@hotmail.it (L.S.); agulino@unict.it (A.G.)
[2] I.N.S.T.M. UdR of Catania, Viale A. Doria 6, 95125 Catania, Italy
* Correspondence: sscire@unict.it; Tel.: +39-095-738-5112

Received: 9 April 2018; Accepted: 9 May 2018; Published: 12 May 2018

Abstract: The catalytic performances of Ru/ceria-based catalysts in the CO preferential oxidation (CO-PROX) reaction are discussed here. Specifically, the effect of the addition of different oxides to Ru/CeO_2 has been assessed. The Ru/CeO_2-MnO_x system showed the best performance in the 80–120 °C temperature range, advantageous for polymer-electrolyte membrane fuel cell (PEMFC) applications. Furthermore, the influence of the addition of different metals to this mixed oxide system has been evaluated. The bimetallic $Ru–Pd/CeO_2$-MnO_x catalyst exhibited the highest yield to CO_2 (75%) at 120 °C whereas the monometallic Ru/CeO_2-MnO_x sample was that one with the highest CO_2 yield (60%) at 100 °C. The characterization data (H_2-temperature programmed reduction (H_2-TPR), X-ray diffraction (XRD), N_2 adsorption-desorption, diffuse reflectance infrared Fourier transform spectroscopy (DRIFT), X-ray photoelectron spectroscopy (XPS)) pointed out that the co-presence of manganese oxide and ruthenium enhances the mobility/reactivity of surface ceria oxygens accounting for the good CO-PROX performance of this system. Reducible oxides as CeO_2 and MnO_x, in fact, play two important functions, namely weakening the CO adsorption on the metal active sites and providing additional sites for adsorption/activation of O_2, thus changing the mechanism from competitive Langmuir–Hinshelwood into non-competitive one-step dual site Langmuir–Hinshelwood/Mars–van Krevelen. As confirmed by H_2-TPR and XPS measurements, these features are boosted by the simultaneous presence of ruthenium and palladium. The strong reciprocal interaction of these metals between them and with the CeO_2-MnO_x support was assumed to be responsible of the promoted reducibility/reactivity of CeO_2 oxygens, thus resulting in the best CO-PROX efficiency at low temperature of the $Ru-Pd/CeO_2$-MnO_x catalyst. The higher selectivity to CO_2 found on the Ru–Pd system, which reduces the undesired H_2 consumption, represents a promising result of this research, being one of the key aims of the design of CO-PROX catalysts.

Keywords: CO preferential oxidation (CO-PROX); fuel cells; ruthenium; palladium; ceria

1. Introduction

The modern energy crisis and urgent development of green technologies and energies have driven in the last decade intensive research in fuel cell technologies both for stationary and mobile uses. In particular, polymer-electrolyte membrane fuel cells (PEMFC), which work in the 80–100 °C temperature range, are among the most promising devices for automotive purposes [1].

The hydrogen used as fuel in PEMFC is currently produced by steam reforming of hydrocarbons or alcohols and a subsequent water–gas shift reaction. The anode of the PEMFC is, however, easily poisoned even at very low concentrations of CO (less than 10 ppm) [2]. Different technologies have

been investigated to purify H_2 from traces of CO including: catalytic methanation [3], membrane separation [4] and preferential oxidation of CO in excess of hydrogen (CO-PROX reaction) [5–7]. The last one, considered highly valuable of investigation, involves two competitive reactions, namely the desired CO oxidation to CO_2 and the undesired H_2 oxidation to water. Therefore, the catalyst of this process must be highly selective towards the first reaction. Noble-metal catalysts, such as Pd [8], Rh [9], Ru [10,11], Au [12–14] and Pt [15,16], have revealed good CO-PROX performance. The selection of the proper support has been also found crucial in addressing the catalytic activity. Recently, the use of a reducible/active support, such as cerium oxide or iron oxide, resulted in remarkably low-temperature CO-PROX activities [12,17]. The peculiar red-ox properties of CeO_2 involving the facile exchange between Ce^{3+} and Ce^{4+} states and the high mobility of O^{2-} ions in the lattice, are the key factors to explain the high relevance of this oxide as a metal support in the PROX reaction [6,12,13,18].

In order to optimize and increase the efficacy of ceria through the rise of the CeO_2 redox properties, one of the most used strategies has been the addition of chemical promoters or the mixing with another oxide such as, for example, CuO [19,20]. In particular, the addition of Mn into a CeO_2 crystal lattice was found to increase the thermal stability and to improve the redox properties of ceria by generating a more efficient Ce^{3+}/Ce^{4+} redox couple [21]. For these reasons, the CeO_2-MnO_x mixed oxides have reported good catalytic activity for various oxidation reactions [22–24]. To the best of our knowledge, few papers deal with the PROX performance of Ru-based catalysts supported on CeO_2 or CeO_2-based materials, although it has been reported that the Ru-based catalysts were more active and selective than Pt-based ones below 150 °C [10,25], an optimal temperature range for a possible use of these catalysts for the hydrogen purification in the PEMFC or for the alkaline fuel cells (AFC).

On the basis of the above considerations, here we report a study of the catalytic performance in the PROX reaction of Ru supported on ceria and ceria-mixed oxide catalysts. In particular, the effect of the addition of another oxide or another metal to Ru/CeO_2 has been explored both in terms of catalytic activity and chemico-physical properties.

2. Results

2.1. Catalytic Activity

A preliminary screening of the PROX activity of monometallic ruthenium catalysts supported on different ceria-based mixed oxides was carried out to determine the best-performing system. The results of investigated monometallic Ru catalysts in terms of CO and O_2 conversions and selectivity and yield towards the CO oxidation as a function of reaction temperature are depicted in Figure 1.

Figure 1a shows the CO conversion against the reaction temperature. Generally, CO conversion on all samples displays a volcano shape behavior as a function of the reaction temperature, i.e., the CO conversion reaches a maximum and then decreases. Reasonably at high temperature, the reverse water–gas shift (RWGS) reaction ($CO_2 + H_2 \leftrightarrow CO + H_2O$) becomes significant (Ea = 120–160 kJ/mol, higher than that found for PROX, 70–100 kJ/mol [5,25]). In fact, on Ru-based catalysts RWGS has been reported to occur at T > 150 °C [10,25], therefore justifying the drop of activity at higher temperatures. Specifically, it is worth noting that the CO conversion upper value and its temperature rely on the mixed-oxide support used. This happens also for selectivity to CO_2 (Figure 1c). To comprehend this behavior, the fact that cerium oxide has a strong tendency to provide active oxygens with strong oxidation power [6,12,25,26], which are however reactive towards both CO and H_2, must be taken into account. This causes a drop of selectivity at higher temperature due to the higher activation energy of H_2 oxidation compared to that of CO [27–30].

Interestingly, the Ru/CeO_2-MnO_x sample exhibited the highest value of CO conversion at lower temperature (70.6% at 100 °C), which is higher than those found for Ru/CeO_2-CuO (62.5% at 170 °C), Ru/CeO_2 (54% at 140 °C) and Ru/CeO_2-Fe_2O_3 (45.6% at 140 °C) samples. In the case of the Ru/CeO_2-CuO catalyst, CO conversion shifted to a higher temperature, probably due to the fact that Cu catalysts require higher temperatures to promote the CO oxidation [12,13,25]. However, it cannot

be fully ruled out that the low activity of the Ru/CeO_2-CuO catalyst can be related to an unsuitable pretreatment of the CuO-CeO_2 system, for which calcination at 450 °C (adopted here for all samples) could not be ideal for the formation of the active Cu^+ sites [19,20].

The Ru/CeO_2 catalyst is, instead, the most active as to the O_2 conversion (Figure 1b), which is due to both CO and H_2 oxidation with 100% conversion reached at about 120 °C, i.e., 50 °C less than on Ru/CeO_2-Fe_2O_3 and Ru/CeO_2-CuO, whereas the Ru/CeO_2-MnO_x sample reached 80.9% conversion at 170 °C. As shown in Figure 1c, the above behavior results in the much higher selectivity of the Ru/CeO_2-MnO_x sample towards the preferential CO oxidation in the 70–140 °C temperature range, with a maximum at 100 °C. This indicates that the contemporaneous presence of reactive oxygens of cerium and manganese oxides leads to a very good selectivity at low temperature. Accordingly, CO_2 yields as a function of temperature (Figure 1d) clearly show that the Ru/CeO_2-MnO_x catalyst is the most efficient among all investigated systems for PROX in the 80–120 °C temperature range.

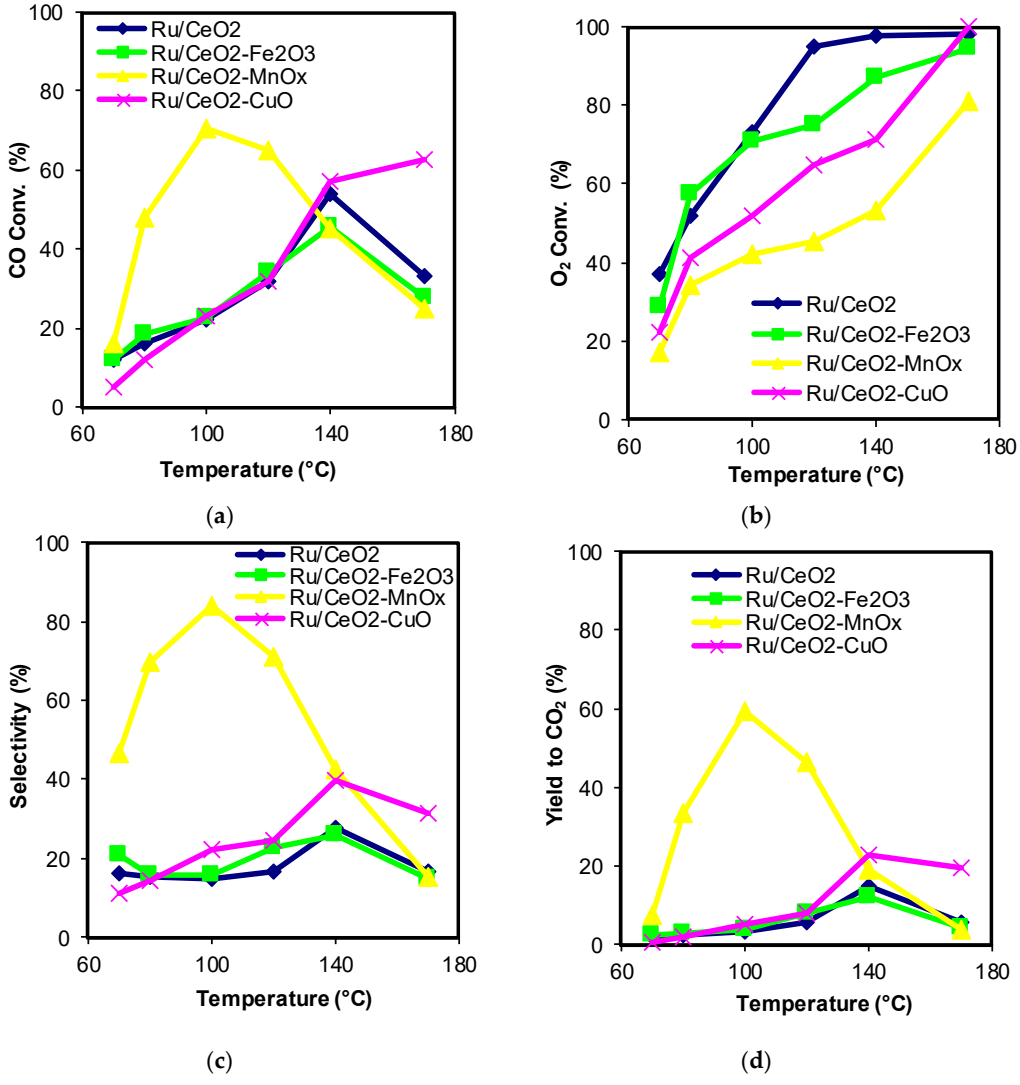

Figure 1. Preferential oxidation (PROX) activity data over monometallic Ru catalysts supported on CeO_2-based mixed oxides. (**a**) CO conversion, (**b**) O_2 conversion, (**c**) selectivity towards CO oxidation, (**d**) yield to CO_2.

The other monometallic samples were far less active, with only the Ru/CeO_2-CuO sample reaching 20% of CO_2 yield in the 140–170 °C temperature range. Therefore, the CeO_2-MnO_x mixed oxide was chosen as a support to investigate other mono (Pt or Pd) and bimetallic (Ru-Pd) catalysts.

Figure 2 displays the CO conversion (Figure 2a), the O_2 conversion (Figure 2b), the selectivity towards the CO oxidation (Figure 2c) and the yield to CO_2 (Figure 2d) of Ru/CeO_2-MnO_x, Pt/CeO_2-MnO_x, Pd/CeO_2-MnO_x and Ru–Pd/CeO_2-MnO_x. The Pd/CeO_2-MnO_x catalyst exhibited an increased CO conversion with the temperature reaching the maximum of 62% at 140 °C whereas the Pt/CeO_2-MnO_x showed the lowest activity in the inspected temperature range (Figure 2a). Pt/CeO_2-MnO_x reached 100% O_2 conversion (Figure 2b) at lower temperature (100–120 °C) compared to Ru/CeO_2-MnO_x and Ru-Pd/CeO_2-MnO_x catalysts; therefore, CO selectivity (Figure 2c) and CO_2 yield (Figure 2d) did not exceed 30%. It is noteworthy that the Ru–Pd system leads to higher CO conversion at high temperature (T > 100 °C) compared to the corresponding monometallic samples (Figure 2a), providing at 120 °C the highest values of CO conversion (85%) (Figure 2a), CO selectivity (88.5%) (Figure 2c), and CO_2 yield (75.3%) (Figure 2d) among all catalysts. It must be stressed that the increased activity of the Ru–Pd system cannot be related to the concentration of the metal species, which on both mono and bimetallic samples remains 1 wt % (0.5–0.5% on bimetallics and 1% on monometallics). It has been seen that bimetallics can be often better performing than the related monometallics due to a synergy between the two metals and/or the support [6,12,31].

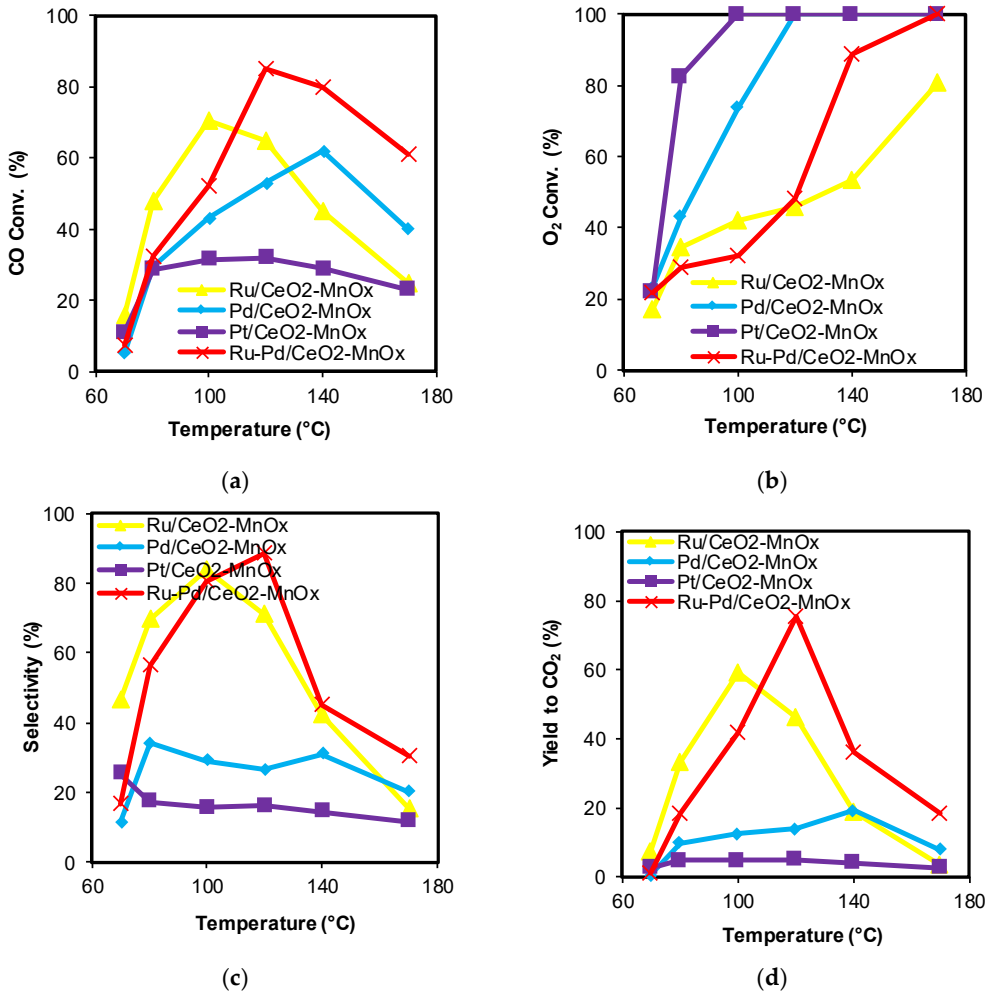

Figure 2. PROX activity data over Ru/CeO_2-MnO_x, Pd/CeO_2-MnO_x, Pt/CeO_2-MnO_x and Ru–Pd/CeO_2-MnO_x catalysts. (**a**) CO conversion, (**b**) O_2 conversion, (**c**) selectivity towards CO oxidation, (**d**) yield to CO_2.

2.2. Catalysts Characterization

In order to find relations between catalytic performances and chemico-physical properties, we investigated the reducibility H_2-temperature programmed reduction (H_2-TPR), the structural and textural properties (diffuse reflectance infrared Fourier transform spectroscopy (DRIFT), X-ray diffraction (XRD) and Brunauer–Emmett–Teller (BET) surface area) and the surface properties (X-ray photoelectron spectroscopy (XPS)) of the most active Ru-based samples.

2.2.1. Temperature Programmed Reduction (H_2-TPR)

Figure 3 shows the H_2-temperature programmed reduction profiles of the analyzed samples between 50 °C and 500 °C. On the bare cerium oxide support, the H_2 consumption starts at around 350 °C, due to the partial reduction of the CeO_2 surface oxygen [12,13]. The reduction of bulk oxygen was reported to take place at temperatures higher than 700 °C [32] and, therefore, is not visible in the TPR curve of Figure 3. The profile of the Ru/CeO_2 sample displays two reduction peaks at 165 °C and 190 °C and a shoulder at ca. 325 °C. According to literature data, the peak at 165 °C is characteristic of the reduction of the ruthenium precursor salt ($Ru(NO)(NO_3)_3$), while the peak at 190 °C is assigned to the reduction of well dispersed ruthenium oxide particles on the surface of the support [10,33]. The shoulder at 325 °C reasonably originates from the reduction of the ceria surface oxygens shifted to lower temperature as a result of the interaction with the ruthenium species.

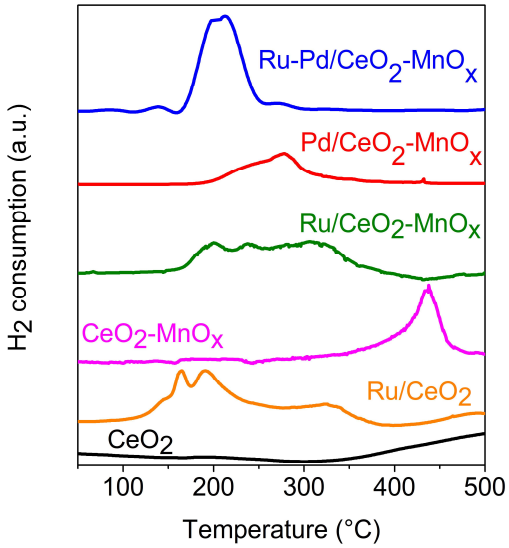

Figure 3. H_2-temperature programmed reduction (H_2-TPR) profiles of investigated catalysts.

A quite sharp reduction peak at 435 °C characterizes the TPR profile of the CeO_2-MnO_x catalyst. In this case, the reduction of ceria surface oxygen is anticipated by the presence of another reducible oxide as MnO_x and probably includes the reduction of MnO_x species to MnO [34–36], as confirmed also by the TPR quantification data (Table S1), being the total H_2 uptake higher (around 1.8 times) than the bare CeO_2. The presence of ruthenium (sample Ru/CeO_2-MnO_x), instead, leads to a wide multi-component peak in the 150–350 °C range, in which it is quite hard to distinguish and attribute with certainty the different reduction signals to each single component (Ru precursor, CeO_2 and MnO_x). The deconvolution procedure (Figure S1A) led to the distinction of three different components at around 199 °C, 246 °C and 314 °C, respectively. Reasonably, considering also the TPR quantification reported in Table S1, the low temperature feature at 200 °C can be attributed to the reduction of the Ru precursor shifted at higher temperature with respect to Ru/CeO_2 due to a stronger metal–support interaction [37]; the signal at around 315 °C can be assigned to the reduction of ceria surface oxygen interacting with ruthenium and manganese oxide; and the feature at 245 °C is probably due to the

reduction of manganese oxide species ($Mn_2O_3 \rightarrow Mn_3O_4$) [36] overlapping with the reduction of dispersed RuO_X particles on the surface of CeO_2-MnO_x. The Pd/CeO_2-MnO_x catalyst shows a wide reduction peak with maximum at circa 275 °C, attributable to the reduction of the PdO-CeO_2-MnO_X species strongly interacting with each other [38,39].

The bimetallic Ru–Pd/CeO_2-MnO_x sample shows a broad peak (around 210 °C) which is at a lower temperature compared to the monometallic palladium catalyst and much more intense than both Ru and Pd monometallics. Furthermore, the total H_2 uptake of Ru–Pd/CeO_2-MnO_x is slightly higher (2106 μmol/g_{cat}) than the sum of the H_2 uptakes of Pd/CeO_2-MnO_x and Ru/CeO_2-MnO_x (2067 μmol/g_{cat}). It is rational to assume that the reduction both of Ru and Pd species, together with that of the superficial oxygens of the mixed CeO_2-MnO_x support, contribute to this peak. The deconvolution of the Ru–Pd/CeO_2-MnO_x reduction peak (Figure S1B) revealed two other contributions, one at low temperature (140 °C) and one at high temperature (275 °C), probably due to the reduction of part of the metal precursors. It is possible in this case, in the same way as other bimetallic systems supported on cerium oxide reported in the literature [6,12], that a mutual interaction between the two metals leads a single reduction peak, distinct from the individual monometallic samples. Furthermore, this reduction peak being shifted at lower temperature than the monometallic Ru sample also suggests an increased reducibility/mobility of the ceria-manganese reactive oxygens [6,12,40].

2.2.2. Structural and Textural Properties

Figure 4 exhibits the XRD patterns of the bare CeO_2 and CeO_2-MnO_x supports and of the Ru/CeO_2, Ru/CeO_2-MnO_x, Pd/CeO_2-MnO_x and Ru-Pd/CeO_2-MnO_x mono and bimetallic samples. The signals at 2θ = 28.6° (1 1 1), 33.1° (2 0 0), 47.5° (2 2 0) and 56.4° (3 1 1) are assigned, according to the Joint Committee on Powder Diffraction Standards (JCPDS) data, to the typical fluorite structure of the CeO_2. No peaks associated with metallic species or manganese oxide were detected. The absence of signals for the Ru and Pd species is plausibly due to the combination of the small size (less than 5 nm) and the low amount (1 wt %) of metals. With regard to manganese oxide, the low amount (5 wt %), the homogeneous distribution of this host oxide on the ceria, and the co-presence of CeO_2 diffraction peaks overlapping with those of manganese oxide, having a similar structure [41], do not allow recognition of variations of the cerium oxide pattern upon addition of MnO_x.

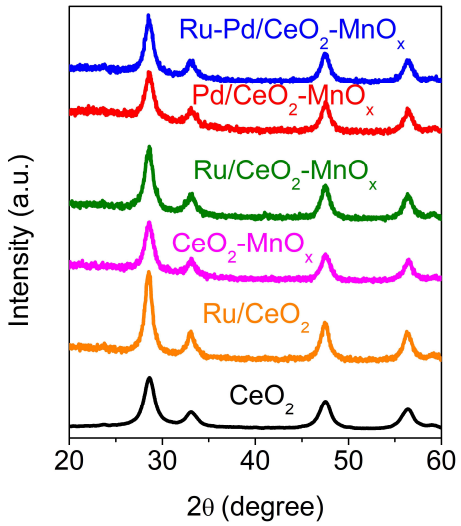

Figure 4. X-ray diffraction (XRD) profiles of investigated catalysts.

The size of the crystalline grains of investigated catalysts, calculated by the Scherrer equation referring to the main peak of cerium oxide at 2θ = 28.6° (1 1 1), their BET surface area and mean pore diameters, calculated with the Dollimore–Heal method [42], are reported in Table 1.

Table 1. Structural and textural properties of investigated samples.

Catalysts	CeO_2 Size by XRD (nm) *	BET Surface Area (m^2/g)	Mean Pore Diameter (nm)	Pore Volume (cm^3/g)
CeO_2	10	107	2.9	0.129
Ru/CeO_2	9.0	108	2.7	0.131
CeO_2-MnO_x	8.5	119	2.1	0.137
Ru/CeO_2-MnO_x	8.8	118	2.2	0.133
Pd/CeO_2-MnO_x	8.7	118	2.3	0.132
Ru-Pd/CeO_2-MnO_x	8.2	123	1.8	0.139

* By Scherrer equation.

The precipitation method with KOH used to synthesize the bare CeO_2 leads to a catalyst with relatively high surface area (107 m^2/g) and small pores (3 nm) in line with literature data [43,44]. A small increase (around 10%) of surface area (119 m^2/g) was noticed in the presence of manganese oxide, consistent with the decrease of the crystallite size (from 10 nm of the bare CeO_2 to 8.5 nm of the mixed CeO_2-MnO_X oxide) and the pore diameter. Interestingly, the bimetallic Ru–Pd/CeO_2-MnO_x sample showed the highest surface area (123 m^2/g) among all investigated samples. It is probable that the presence of a bimetallic phase, well spread on the mixed ceria-manganese oxide, favours the replacement of cerium ions with manganese ones in the fluorite structure, which is reasonably due to the crystal structure similarity [41]. Moreover, a part of the well dispersed bimetallic components can move into the interlayers of the ceria support.

The DRIFT spectrum (4000–500 cm^{-1}) of the cerium oxide support is shown in Figure S2. On the basis of the literature, the signal at 3470 cm^{-1} can be assigned to the O–H stretching of H-bonded water [45]. The bands at 1585 and 1346 cm^{-1} are due to the O–C–O stretching vibrations whereas the features at 1057 and 852 cm^{-1} can be assigned to the C–O stretching, thus pointing to the presence of carbonate species on the oxide sample. Finally, the band at 600 cm^{-1} can be attributed to the O–Ce–O phononic vibration of the crystal lattice of the cerium oxide [46]. Figure 5a compares the DRIFT spectrum of the support with those of the investigated samples. It is evident that all mixed oxides reveal a shift of the bands assigned to carbonates. This is better highlighted in Figure 5b, where the zoomed 1800–1000 cm^{-1} region is reported. The presence of different carbonate species is typical of basic oxide materials, such as cerium oxide, owing to the interaction of basic sites with the atmospheric CO_2 [43,44]. The inspection of literature data [47–49] points to the presence of variously coordinated carbonate species (O–C–O asymmetrical and symmetrical stretchings at 1600–1470 cm^{-1} and 1370–1300 cm^{-1}, respectively) and un-coordinated H-bonded carbonate (ν_{as} CO_3^{2-} at 1450–1420 cm^{-1}). In the case of the CeO_2 samples (CeO_2 and Ru/CeO_2), the coordinated carbonate bands were predominant, whereas for the CeO_2-MnO_x supported samples (CeO_2-MnO_x, Ru/CeO_2-MnO_x, Pd/CeO_2-MnO_x and Ru-Pd/CeO_2-MnO_x) the un-coordinated H-bonded carbonate band was the main feature. This behaviour suggests that the presence of manganese oxide significantly modified the acid-base properties of the system, causing a decrease of the basicity of the oxide support, thus strongly affecting the nature of CO_2 adsorption sites.

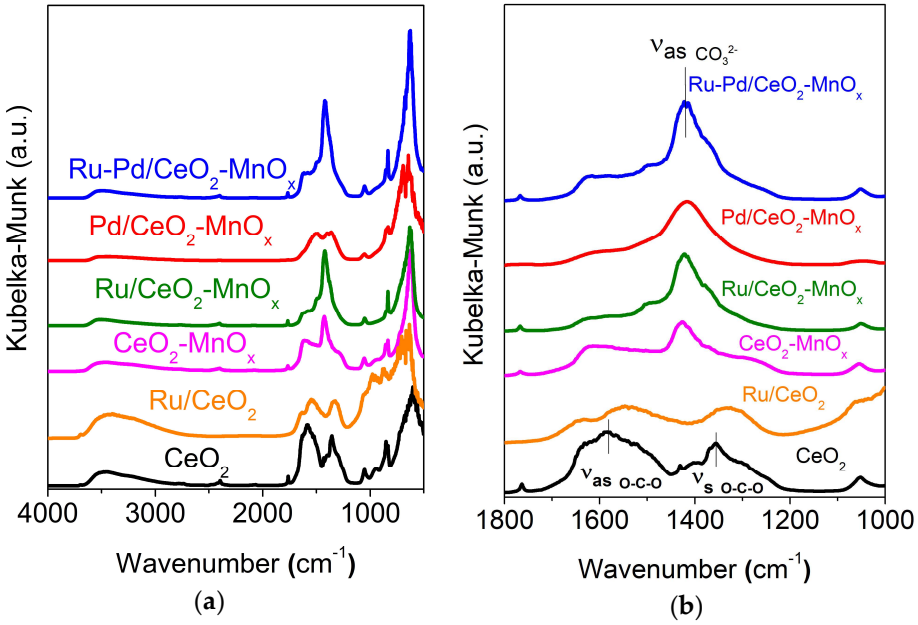

Figure 5. Diffuse reflectance infrared Fourier transform (DRIFT) spectra of catalysts: (**a**) CeO_2-based catalysts, (**b**) zoom of the carbonate zone.

2.2.3. X-ray Photoelectron Spectroscopy (XPS) Measurements

The electronic structure of the Ru/CeO_2, Ru/CeO_2-MnO_x and $Ru–Pd/CeO_2$-MnO_x samples was investigated by XPS, which provides information on the surface elemental composition, the oxidation status and the chemical surroundings of the studied species [50,51].

The Ru 3d states (Figure S3) overlap the C 1s levels, so we prefer to mainly discuss the XPS of the Ru 3p binding-energy region. The two Ru $3p_{3/2,1/2}$ spin-orbit components for Ru/CeO_2 (Figure 6a) lie at 462.7 and 485.1 eV, respectively. These energy values and also the Ru $3d_{5/2}$ state, at 281.3 eV (Figure S3), are indicative of the presence of RuO_2 on the surface sample [52–55]. RuO_2 is also present on the surface sample of Ru/CeO_2-MnO_x since the Ru $3d_{5/2}$ state is at 281.5 eV and the two Ru $3p_{3/2,1/2}$ spin-orbit components are at 463.3 and 485.8 eV, respectively. It is important to stress that XPS is a surface-sensitive technique that probes a thickness of ~60 Å in our conditions. The above energy values are significantly lower in the case of $Ru–Pd/CeO_2$-MnO_x, being the Ru $3d_{5/2}$ state at 280.8 eV and the two Ru $3p_{3/2,1/2}$ spin-orbit components at 462.2 and 484.6 eV, respectively. All these latter values are consistent with the presence of metallic Ru in the $Ru–Pd/CeO_2$-MnO_x sample [56].

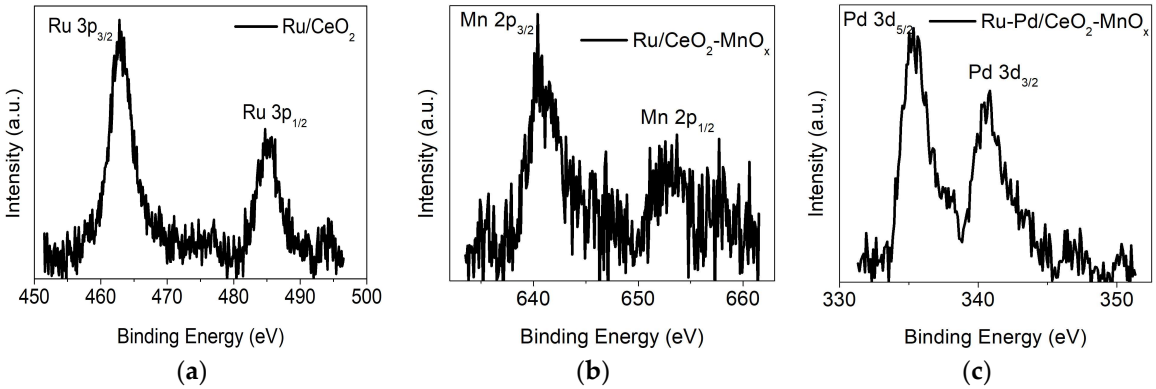

Figure 6. X-ray photoelectron spectroscopy (XPS) of catalysts: (**a**) Ru/CeO_2 in the Ru 3p energy region, (**b**) Ru/CeO_2-MnO_x in the Mn 2p energy region, (**c**) $Ru–Pd/CeO_2$-MnO_x in the Pd 3d energy region.

The Mn $2p_{3/2,1/2}$ spin-orbit levels are at 640.4 and 652.4 eV (Figure 6b), respectively, in both Ru/CeO_2-MnO_x and Ru–Pd/CeO_2-MnO_x systems. Moreover, there is evidence of satellite features at ~7 eV higher binding energy from the main peaks that are a fingerprint of the presence of MnO, since these satellites are absent in Mn_2O_3 and in MnO_2 species [57].

Finally, Figure 6c shows the XPS of the Pd 3d states for the Ru–Pd/CeO_2-MnO_x system. The binding energy values of 335.3 and 340.6 due to the Pd $3d_{5/2,3/2}$ spin-orbit components can be unambiguously assigned to metallic palladium [58–60]. It must be noted that the full width at half maximum (FWHM) of the Ru $3p_{3/2}$ states for the Ru/CeO_2 (Figure 6a) is 1.8 eV, that of the Mn $2p_{3/2}$ states for the Ru/CeO_2-MnO_x (Figure 6b) is 1.65 eV and that of the Pd $3d_{5/2}$ states for the Ru–Pd/CeO_2-MnO_x (Figure 6c) is 1.1 eV.

In all cases, the CeO_2 system gave the expected XPS 3d signals as reported in Figure S4. Concerning the Ce(IV)/Ce(III) ratio, it must be noted that peaks at 882.0, 888.6 and 897.9 eV (Figure S4) are from the Ce $3d_{5/2}$ states and peaks at 900.5, 906.9 and 916.2 are from the $3d_{3/2}$ states. The first two peaks at 882.0 and 888.6 eV are due to a mixing configuration of $3d^94f^2(O\ 2p^4)$ and $3d^94f^1(O\ 2p^5)$ Ce^{4+} states, and the peak at 897.9 eV belongs to the $3d^94f^0(O\ 2p^6)$ Ce^{4+} state. The series of peaks at 900.5, 906.9 and 916.2 are the related spin-orbit components of the $3d_{3/2}$ states of the same configurations. Moreover, there is no structure between the peaks at 882.0 eV, 888.6 eV and 897.9 eV, and this rules out any $3d^94f^1(O\ 2p^6)$ Ce^{3+} final state [61].

The O1s peaks of the representative Ru/CeO_2 can be fitted into two peaks referred to as the lattice oxygen O^{2-} and the chemisorbed OH^- groups. The O1s peak at about 528.7 eV is due to the lattice oxygen (O^{2-}) for CeO_2, and that at 530.6 eV belongs to the chemisorbed OH^- species. In the case of the Ru/CeO_2-MnO_x the energy positions of these two peaks are 528.9 and 530.4 eV while in the case of Ru–Pd/CeO_2-MnO_x these two peaks lie at 529.2 and 530.8 eV. The intensity ratio between these two peaks (1.2–1.3) is almost the same in all the three different investigated systems, thus excluding different affluent oxygen species on the samples surface [61]. The deconvolution features are reported in the supporting information (Figure S5).

The XPS atomic concentration analysis of the three investigated systems clearly show some surface segregation of ruthenium [62] since the Ru/Ce is 0.18, 0.12 and 0.06 for the Ru/CeO_2, Ru/CeO_2-MnO_x and Ru–Pd/CeO_2-MnO_x systems, respectively. The Mn/Ce is 0.07 and 0.03 for the Ru/CeO_2-MnO_x and Ru–Pd/CeO_2-MnO_x systems, respectively and, finally, the Pd/Ce is 0.02 for the Ru–Pd/CeO_2-MnO_x system. XPS also indicates that there is neither nitrogen, potassium nor chlorine signals in all these samples, thus inferring the purity of the samples with respect to the starting reagents (see Figure S6 with the survey spectrum of the Ru/CeO_2 sample).

3. Discussion

In this paper the catalytic activity of ceria-based mixed oxides (CeO_2-Fe_2O_3, CeO_2-CuO and CeO_2-MnO_x) supported mono and bimetallic Ru-Pd samples was evaluated in the CO-PROX reaction. A preliminary comparison of the catalytic results among investigated mixed oxides supported Ru monometallic catalysts pointed out that the Ru/CeO_2-MnO_x sample was the most selective towards the CO oxidation (Figure 1c), providing the highest CO_2 yield (Figure 1d) in the temperature range of PEM fuel cells (80–120 °C). Therefore, the CeO_2-MnO_x mixed oxide was chosen for further investigation focusing on Ru–Pd bimetallic systems.

As reported in the literature [63,64], the manganese oxide is a reducible oxide as ceria, and then it can provide, in addition to those of CeO_2, beneficial reactive oxygens for oxidation reactions. Moreover, CeO_2-MnO_x mixed oxides can also show stronger redox properties than CeO_2 alone, due to the multi-valence surface state and the mutual contact between ceria and manganese oxide [65,66]. It has been reported that the oxygen storage capacity of CeO_2 is boosted by the presence of manganese oxide, with the surface oxygen mobility of ceria also improved by forming MnO_x-CeO_2 solid solution [67]. In our case, the occurrence of an interaction between ruthenium-CeO_2 and MnO_x itself, proved by TPR data, can be one of the reasons for the excellent performance of this catalyst in the CO-PROX reaction. Interestingly, the Ru/CeO_2-MnO_X exhibited better performance compared to the other investigated monometallic systems

(Pt and Pd, Figure 2). Furthermore, the Ru–Pd/CeO_2-MnO_x system showed higher selectivity (Figure 2c) and yield to CO_2 (Figure 2d) compared to the Ru/CeO_2-MnO_x catalyst at T > 100 °C, namely in the operative range of alkaline fuel cells (100–140 °C).

To elucidate the catalytic behavior of the investigated catalysts it is important to refer to the CO-PROX reaction mechanisms reported in the literature for reducible oxide-supported metal catalysts [5] and for non-reducible oxide-supported Ru catalysts [10].

For reducible oxide-supported metal catalysts, it was stated that the reaction occurs between CO and oxygen co-adsorbed on the surface-active sites. The oxygen can be activated at the metal/support-oxide interface and/or the reducible surface oxygens of the oxide can participate in the reaction [5]. However, it is necessary to clarify that a greater activation of oxygen does not directly mean a better yield for CO oxidation reactions: activated oxygen can in fact react with both CO and H_2, which means that the two species are in strong competition between each other for the oxidation reaction. In order to obtain a good yield, it is then necessary to activate CO and not H_2. It is well known that cerium oxide has good catalytic properties for oxidation reactions, since it has mobile/reducible oxygens [6,12,13,43,68]. The mobility of such oxygens can be increased by the presence of metals on the surface, which introduce crystalline defects that increase the mobility of these oxygens and increasing the oxidative power of the substrate [12,43,67]. Specifically, for the preferential oxidation of CO the most widely reported mechanism is that of Mars–van Krevelen (MvK) [6,13,43,68–70]. The aforesaid mechanism involves different reaction steps: the first is the formation of a chemical bond between the reagents (CO, O_2 or H_2) and the catalyst surface; then the formation and the desorption of products (CO_2 and H_2O) take place with the generation of oxygen vacancies in the bulk of the ceria, which can then be replaced by the subsequent oxygen adsorption from the gaseous phase. In this case, an important parameter is the reactivity of the support oxide (ceria) oxygens, which are directly involved in the reaction, being able to react at the metal/CeO_2 interface with CO to form CO_2. The reducibility of the cerium oxide reflects directly the mobility and therefore the reactivity of surface oxygens with an increased reducibility (mobility/reactivity) beneficial for the catalytic activity in the CO-PROX reaction [5,6,12,13,43,68–70].

For ruthenium or platinum-based catalysts supported on non-reducible (inert) oxides, as reported in the literature, the oxidation of CO occurs according to the Langmuir–Hinshelwood mechanism [71,72]. Both reagents (CO and O_2) bind to the surface at the active sites of the metal species. In particular, the following mechanism was assumed on ruthenium-based catalysts:

(a) Reactants' adsorption on the Ru surface:

$$CO_{(g)} + Ru \rightarrow CO_{ad}\text{-}Ru$$
$$O_{2(g)} + Ru \rightarrow O_{2(g)}\text{-}Ru$$

(b) Oxygen dissociation:

$$O_{2(g)}\text{-}Ru \rightarrow O_{ad}\text{-}Ru$$

(c) CO_2 formation:

$$CO_{ad}\text{-}Ru + O_{ad}\text{-}Ru \rightarrow CO_{2(g)}\text{-}Ru$$

However, also in this case, it must be considered that the reaction mixture of CO-PROX contains considerable hydrogen excess (88 vol. %) and, therefore, H_2 can also be activated by the metal surface sites, thus competing with CO in reacting with oxygen and influencing the selectivity of the CO-PROX reaction [10,73].

The mobility of the ceria oxygens can be increased both by interaction with a metal and by the presence of a host oxide [44,74,75]. From the TPR characterization (Figure 3), it is possible to infer that a strong interaction is established between Ru–Pd and the mixed oxide CeO_2-MnO_x support, thus enhancing the reducibility/reactivity of the ceria oxygens (the reduction peak of the bimetallic sample is at a lower temperature and more intense than the corresponding monometallic ones). This can explain the higher activity of this catalyst. As evidenced by the XRD measurements in both the monometallic and

bimetallic samples, the small metal particle size (below 5 nm of diameter) and the good distribution of manganese oxide on the ceria can be decisive factors in explaining the excellent catalytic performances of Ru/CeO_2-MnO_x and $Ru–Pd/CeO_2$-MnO_x catalysts. The strong interaction between Ru–Pd and the mixed oxide CeO_2-MnO_x was, furthermore, confirmed by XPS measurements, with the $Ru–Pd/CeO_2$-MnO_x sample that showed the presence of metallic Ru and Pd species on the surface of the sample a key factor explaining the higher activity of this sample compared to the Ru/CeO_2-MnO_x and Ru/CeO_2 samples where Ru^{4+} species were also detected. As reported in the literature, metallic Ru^0 is more active compared to oxidized Ru^{n+} species [76,77]. In this case, the simultaneous presence of Pd^0 also facilitates the redox process of the ceria-manganese oxide, thus favouring an easier CO activation.

To interpret the results obtained, it is then reasonable to hypothesize a mixed Langmuir–Hinshelwood/Mars–van Krevelen (LH/MvK) reaction mechanism. In this case, in fact, the reaction can take place in one step: the adsorbed CO (CO_{ad}) reacts very quickly with the mobile/active oxygens of the mixed CeO_2-MnO_x oxide, also allowing the rapid desorption of the CO_2 produced, while the oxygen vacancy is instantly replaced by the O_2 adsorbed. The fast desorption of the produced CO_2 can be favoured by the modification of the surface sites of the CeO_2-MnO_x with respect to the cerium oxide as revealed by the DRIFT data (Figure 5), while the adsorption of oxygen and CO from the gas phase is allowed by the increased surface area of the mixed oxide (Table 1).

In conclusion, the use of the mixed cerium-manganese oxide system allows excellent performance to be obtained in the preferential oxidation reaction of CO due, essentially, to: (1) a higher reducibility/reactivity of the ceria surface oxygen; (2) a higher surface area which favours an easier and fast adsorption of the reacting species and a faster desorption of the CO_2 produced, due also to the modification of the surface adsorption sites. The strong interaction of the mixed oxide with Ru in the monometallic Ru/CeO_2-MnO_x and the effective synergism between Ru and Pd in the Ru–Pd bimetallic system allows the design of proper catalysts for the specific use of H_2 purification in fuel cells working at low temperature (PEM and AFC). In particular, the Ru/CeO_2-MnO_x catalyst appears the most suitable for PEM fuel cells (operating temperature range of 80–120 °C) while the $Ru–Pd/CeO_2$-MnO_x system can be considered best for the AFC fuel cells (operating temperature range of 100–140 °C). It is interesting to note that the catalytic performances of these catalysts were comparable or even better, in terms especially of CO_2 selectivity, with respect to ceria and ceria-manganese oxide-based catalysts reported in the literature for CO-PROX (see Table 2) [12,78–82], even though it must stressed that a realistic comparison is very difficult due to the different operative conditions of the various works. As displayed in Figure 7, the Ru/CeO_2-MnO_x and Ru-Pd/CeO_2-MnO_x catalysts were quite stable after 14 h of streaming both at 100 °C and 120 °C, whereas the monometallic Pd sample began to deactivate at 120 °C after 8 h. The higher selectivity to CO_2 found on the Ru–Pd system, which reduces the undesired H_2 consumption, represents a promising result of this research, being one of the key aims of the design of CO-PROX catalysts.

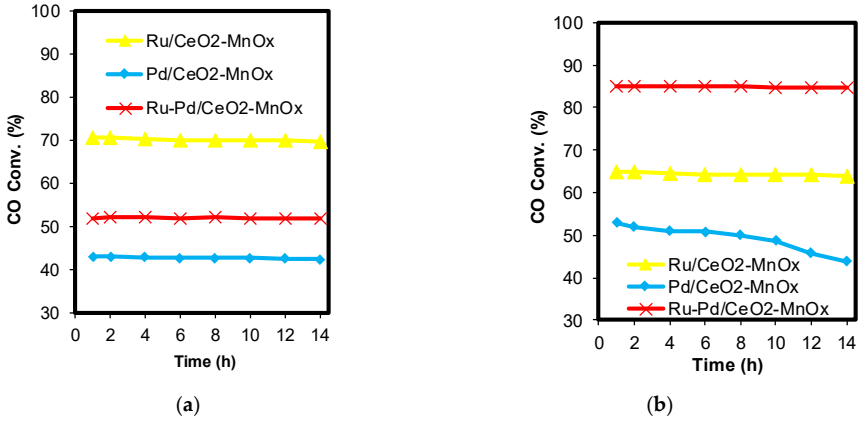

Figure 7. Conversion of CO as a function of time on stream at 100 °C (**a**) and 120 °C (**b**) over Ru/CeO_2-MnO_x, Ru/CeO_2-MnO_x and Ru/CeO_2-MnO_x catalysts.

Table 2. Comparison of PROX performance of Ru and Ru–Pd supported CeO_2-MnO_x catalysts in this work and other ceria and ceria-manganese oxide-based catalysts reported in the literature.

Catalysts	Metals Loading (wt %)	Support	Space Velocity (GHSV)	Gas Mixture (vol. %)	CO Conversion (%)	CO_2 Selectivity (%)	Ref.
Ru/CeO_2-MnO_x	1	CeO_2-5wt%MnO_x	0.39 mol_{CO} h^{-1} $g_{cat}{}^{-1}$	1 CO, 1 O_2, 88 H_2, rest He	41 (80 °C) 72 (100 °C) 65 (120 °C)	70 (80 °C) 84 (100 °C) 71 (120 °C)	this work
Ru–Pd/CeO_2-MnO_x	0.5–0.5	CeO_2-5wt%MnO_x	0.39 mol_{CO} h^{-1} $g_{cat}{}^{-1}$	1 CO, 1 O_2, 88 H_2, rest He	32 (80 °C) 52 (100 °C) 85 (120 °C)	56 (80 °C) 81 (100 °C) 88 (120 °C)	this work
Pt/CeO_2	1	CeO_2	not reported	1 CO, 1 O_2, rest H_2	65 (80 °C) 70 (100 °C) 60 (120 °C)	72 (80 °C) 68 (100 °C) 61 (120 °C)	[78]
Rh/MnO_2-CeO_2/Al_2O_3	1	10 wt %MnO_2, 40 wt %CeO_2, 50 wt %Al_2O_3	60,000 cm^3 h^{-1} $g_{cat}{}^{-1}$	1 CO, 1 O_2, 50 H_2, rest N_2	15 (80 °C) 20 (100 °C) 38 (120 °C)	57 (80 °C) 55 (100 °C) 50 (120 °C)	[79]
CeO_2/Co_3O_4-MnO_2/CeO_2	-	27.5 wt %Co on activated carbon 8:1 Co/Mn and Co/Ce (atom. ratio)	15,000 mL h^{-1} $g_{cat}{}^{-1}$	1 CO, 1 O_2, 50 H_2, rest Ar	82 (80 °C) 100 (100 °C) 100 (120 °C)	85 (80 °C) 80 (100 °C) 70 (120 °C)	[80]
Au/MnO_2-CeO_2	1	0.5MnO_2 0.5CeO_2 (atom. ratio)	not reported	1.33 CO, 1.33 O_2, 65.33 H_2, rest He	90 (80 °C) 88 (100 °C) 86 (120 °C)	50 (80 °C) 47 (100 °C) 45 (120 °C)	[81]
CuO/CeO_2	6	PMMA as template	22,000 h^{-1}	1.25 CO, 1.25 O_2, 50% H_2, rest He	92 (80 °C) 96 (100 °C) 97 (120 °C)	82 (80 °C) 80 (100 °C) 78 (120 °C)	[82]
Au-Ag/CeO_2	1–1	CeO_2	0.39 mol_{CO} h^{-1} $g_{cat}{}^{-1}$	1 CO, 1 O_2, 88 H_2, rest He	90 (80 °C) 76 (100 °C) 50 (120 °C)	73 (80 °C) 44 (100 °C) 30 (120 °C)	[12]

4. Materials and Methods

4.1. Catalyst Preparation

The bare cerium oxide support was synthesized upon precipitation with KOH (1 M) (Fluka, Buchs, Switzerland) from a water solution of $Ce(NO_3)_3 \cdot 6H_2O$ (Fluka, Buchs, Switzerland), subsequent filtration, washing with water to ensure the removal of nitrates, and final calcination of the obtained solid at 450 °C in air for 4 h. Mixed oxides (CeO_2-5wt%Fe_2O_3, CeO_2-5wt%MnO_x and CeO_2-5wt%CuO) were obtained by co-precipitation with KOH following the same procedure used for the bare CeO_2, adding together with the solution of $Ce(NO_3)_3 \cdot 6H_2O$ the stoichiometric amount of $Fe(NO_3)_3 \cdot 9H_2O$ (Fluka, Buchs, Switzerland), $Mn(NO_3)_2 \cdot 4H_2O$ (Fluka, Buchs, Switzerland) or $Cu(NO_3)_2 \cdot 6H_2O$ (Riedel-de Haën, Seelze, Germany).

The preparation of Ru/CeO_2 and Ru/CeO_2-mixed oxide catalysts (1 wt % Ru) was achieved by incipient wetness impregnation of the supports with an aqueous solution of the ruthenium precursor ($Ru(NO)(NO_3)_3$) (Alfa Aesar, Haverhill, MA, USA). In particular, the stoichiometric amount of $Ru(NO)(NO_3)_3$ was added dropwise to the support, to fill the pores. The slurry then obtained was placed in an oven at 110 °C to evaporate the excess of solvent. This process was repeated until addition of the required amount of $Ru(NO)(NO_3)_3$. Finally, the sample was dried overnight at 110 °C.

The same procedure was adopted for Pd (1 wt % Pd), Ru-Pd (0.5 wt % Ru, 0.5 wt % Pd) and Pt (1 wt % Pt) catalysts using $PdCl_2$ (Sigma-Aldrich, Buchs, Switzerland) and/or $H_2PtCl_6 \cdot 6H_2O$ (Alfa Aesar, Haverhill, MA, USA) as metal salt precursors for palladium and platinum, respectively. In the case of bimetallic samples, the metal precursors were added contemporaneously on the CeO_2-MnO_x support.

4.2. Catalytic Performance Test

Catalytic activity runs were executed in the gas phase at atmospheric pressure in a continuous flow mode, using a reactor loaded with the catalyst (0.05 g, 80–140 mesh) and 0.45 g of an inert

glass powder. Catalysts were pre-reduced in H_2 at 350 °C. The gas mixture (80 mL/min) was $CO/O_2/He/H_2$ (1/1/10/88 vol. %). A gas hour space velocity of 3.92×10^{-2} mol_{CO} h^{-1} $g_{cat}{}^{-1}$ was chosen. The effluent gases were analyzed online with gas chromatography (Trace GC, Thermo Finnigan, Waltham, MA, USA) with a Carboxen 1000 packed column and TCD detector.

CO and O_2 conversions were estimated from the ratio of the consumed to the initial amount of each gas, whereas selectivity was determined in terms of ratio of O_2 used for the CO oxidation and the whole O_2 consumed, according to the subsequent formulas:

$$\text{CO conversion (\%)} = ([CO_2]_{out}/[CO]_{in}) \times 100$$
$$O_2 \text{ conversion (\%)} = (([O_2]_{in} - [O_2]_{out})/[O_2]_{in}) \times 100$$
$$\text{Selectivity (\%)} = (0.5 \times [CO_2]_{out}/([O_2]_{in} - [O_2]_{out})) \times 100$$
$$CO_2 \text{ yield (\%)} = (\text{Selectivity} * \text{CO conversion})/100$$

4.3. Catalysts' Characterization

H_2-TPR was carried out heating 0.05 g of the sample (dried in a oven at 110 °C) at 10 °C min^{-1} in a home-made flow apparatus with a TCD detector using 5 vol. % H_2 in Ar [10]. The system employed an oxygen adsorbent to purify the reducing mixture and an acetone trap (−80 °C) to block the water and other gases released during TPR.

X-ray photoelectron spectra (XPS) of the powder samples, compressed on indium foil were measured with a PHI 5600 Multi Technique System (Chanhassen, MN, USA) (base pressure of the main chamber 3×10^{-8} Pa) [83,84]. Samples were excited with the Al-Kα X-ray radiation using a pass energy of 5.85 eV. The instrumental energy resolution was ≤0.5 eV. XPS peak intensities were obtained after a Shirley background removal. Spectra calibration was achieved by fixing the main C 1s peak at 285.0 eV. Structures due to the Al-Kα X-ray satellites were subtracted prior to data processing. The atomic concentration analysis was performed by taking into account the relevant atomic sensitivity factors. The fittings of the C 1s and O 1s XP spectra were carried out using Gaussian envelopes after subtraction of the background until there was the highest possible correlation between the experimental spectrum and the theoretical profile. The residual or agreement factor R, defined by $R = [\Sigma(F_{obs} - F_{calc})^2/\Sigma(F_{obs})^2]^{1/2}$, after minimization of the function $\Sigma(F_{obs} - F_{calc})^2$, converged to the value of 0.02. The catalysts for XPS measurements were introduced in the XPS antechamber under vacuum as soon as they were reduced in H_2 at 350 °C.

Diffuse reflectance infrared (IR) spectra were recorded in the range 4000–600 cm^{-1} with a Perkin-Elmer FT-IR System 2000 (Perkin-Elmer, Waltham, MA, USA) using the specific set-up and mirrors for the diffuse reflectance measurements, KBr being employed to obtain the background spectrum.

XRD analysis was performed with a Bruker AXSD5005 (Bruker, Karlsruhe, Germany) X-ray diffractometer using a Cu Kα radiation. Peaks of crystalline phases were compared with those of standard compounds reported in the JCPDS Data File (Bruker, Diffrac. Suite™ Software package, Karlsruhe, Germany). Before the measurements, the well-grounded samples were placed in the powder sample holder. The analysis was made in locked couple mode.

Surface area determination was achieved with a Sorptomatic series 1990 (Thermo Quest, Milano, Italy) adopting the BET N_2 adsorption method. All samples were previously outgassed (10^{-3} Torr) at 120 °C.

5. Conclusions

Different CeO_2-mixed oxides were synthesized by the co-precipitation method and ruthenium was subsequently added by incipient wetness impregnation. Among monometallic samples, the Ru/CeO_2-MnO_x catalyst showed the highest activity in the CO-PROX reaction at 100 °C. The performance of the bimetallic Ru–Pd system on the ceria-manganese support was successively studied. The bimetallic sample exhibited the highest CO_2 yield at 120 °C. On the basis of characterization data, a one-step Langmuir–Hinshelwood/Mars–van Krevelen mechanism was

proposed. The high mobility of ceria surface oxygens was enhanced by the simultaneous presence of manganese oxide and ruthenium. The increased reducibility/reactivity of CeO_2 oxygen was further promoted by the occurrence of a strong interaction between ruthenium and palladium, resulting in an increased CO-PROX activity of the Ru–Pd/CeO_2-MnO_x catalyst.

Supplementary Materials: The following are available online at http://www.mdpi.com/2073-4344/8/5/203/s1, Figures S1: H_2-TPR profiles with peaks deconvolution for Ru/CeO_2-MnOx (A) and Ru-Pd/CeO_2-MnOx (B) samples; Table S1. H_2-TPR quantification for the investigated catalysts; Figure S2. Drift spectra of bare CeO_2; Figure S3. Al Kα excited XPS of the 1% Ru/CeO_2 in the Ru 3d – C 1s energy region. The peak at 281.3 eV is due to the Ru 3d5/2 state, the peak at 285.0 eV is due both to the adventious carbon and Ru 3d3/2 state; Figure S4. Al Kα excited XPS of the Ru/CeO_2 in the Ce 3d energy region; Figure S5A. Al Kα excited XPS of the Ru/CeO_2 in the Ru 3d – C 1s energy region; the black line refers to the experimental profile; the green line refers to the background; the peaks at 281.3 and 285.4 eV (blue line) represent the Ru 3d5/2,3/2 spin-orbit components, the peak at 285.0 eV (cyan line) refers to the adventitious carbon; the red line, superimposed to the experimental profile, refers to the sum of the Gaussian components; Figure S5B. Al Kα excited XPS of the Ru/CeO_2 in the O 1s energy region. The black line refers to the experimental profile; the green line refers to the background; the cyan line refers to the 528.7 eV peak; the blue line refers to the 530.6 eV peak; the red line, superimposed to the experimental profile, refers to the sum of the Gaussian components; Figure S6. XPS survey spectrum of Ru/CeO_2.

Author Contributions: R.F. planned and performed the catalytic experiments and H_2-TPR, DRIFT and N_2-adsorption-desorption measurements, A.G. and L.S. performed and discussed the XPS analysis, S.S. conceived the idea of writing the paper, supervised the work and edited the article.

Acknowledgments: The authors would like to acknowledge the research group of G.G. Condorelli (University of Catania) for the XRD measurements.

Conflicts of Interest: The authors declare no conflict of interest.

References

1. Kim, D.J.; Jo, M.J.; Nam, S.Y. A review of polymer-nanocomposite electrolyte membranes for fuel cell application. *J. Ind. Eng. Chem.* **2015**, *21*, 36–52. [CrossRef]
2. O'Connel, M.; Kolb, G.; Schelhaas, K.; Schuerer, J.; Tiemann, D.; Ziogas, A.; Hessel, V. The development and evaluation of microstructured reactors for the water gas shift and preferential oxidation reactions in the 5 kW range. *Int. J. Hydrog. Energy* **2010**, *35*, 2317–2327. [CrossRef]
3. Park, E.D.; Lee, D.; Lee, H.C. Recent progress in selective CO removal in a H_2-rich stream. *Catal. Today* **2009**, *139*, 280–290. [CrossRef]
4. Tosti, S. Overview of Pd-based membranes for producing pure hydrogen and state of art at ENEA laboratories. *Int. J. Hydrog. Energy* **2010**, *35*, 12650–12659. [CrossRef]
5. Liu, K.; Wang, A.; Zhang, T. Recent Advances in Preferential Oxidation of CO Reaction over Platinum Group Metal Catalysts. *ACS Catal.* **2012**, *2*, 1165–1178. [CrossRef]
6. Fiorenza, R.; Crisafulli, C.; Condorelli, G.G.; Lupo, F.; Scirè, S. Au–Ag/CeO_2 and Au–Cu/CeO_2 Catalysts for Volatile Organic Compounds Oxidation and CO Preferential Oxidation. *Catal. Lett.* **2015**, *145*, 1691–1702. [CrossRef]
7. Nguyen, T.S.; Morfin, F.; Aouine, M.; Bosselet, F.; Rousset, J.L.; Piccolo, L. Trends in the CO oxidation and PROX performances of the platinum-group metals supported on ceria. *Catal. Today* **2015**, *253*, 106–114. [CrossRef]
8. Mariño, F.; Descorme, C.; Duprez, D. Noble metal catalysts for the preferential oxidation of carbon monoxide in the presence of hydrogen (PROX). *Appl. Catal. B Environ.* **2004**, *54*, 59–66. [CrossRef]
9. Kim, Y.H.; Park, E.D.; Lee, H.C.; Lee, D.; Lee, K.H. Preferential CO oxidation over supported noble metal catalysts. *Catal. Today* **2009**, *146*, 253–259. [CrossRef]
10. Sciré, S.; Fiorenza, R.; Gulino, A.; Cristaldi, A.; Riccobene, P.M. Selective oxidation of CO in H_2-rich stream over ZSM5 zeolites supported Ru catalysts: An investigation on the role of the support and the Ru particle size. *Appl. Catal. A Gen.* **2016**, *520*, 82–91. [CrossRef]
11. Di, L.; Wu, G.; Dai, W.; Guan, N.; Li, L. Ru/TiO_2 for the preferential oxidation of CO in H_2-rich stream: Effects of catalyst pre-treatments and reconstruction of Ru sites. *Fuel* **2015**, *143*, 318–326. [CrossRef]
12. Fiorenza, R.; Crisafulli, C.; Scirè, S. H_2 purification through preferential oxidation of CO over ceria supported bimetallic Au-based catalysts. *Int. J. Hydrog. Energy* **2016**, *41*, 19390–19398. [CrossRef]

13. Scirè, S.; Crisafulli, C.; Riccobene, P.M.; Patanè, G.; Pistone, A. Selective oxidation of CO in H_2-rich stream over Au/CeO_2 and Cu/CeO_2 catalysts: An insight on the effect of preparation method and catalyst pretreatment. *Appl. Catal. A Gen.* **2012**, *417–418*, 66–75. [CrossRef]
14. Ilieva, L.; Petrova, P.; Pantaleo, G.; Zanella, R.; Sobczak, J.W.W.; Lisowski, W.; Kaszkur, Z.; Munteanu, G.; Yordanova, I.; Liotta, L.F.; et al. Alumina supported Au/Y-doped ceria catalysts for pure hydrogen production via PROX. *Int. J. Hydrog. Energy* **2018**, in press. [CrossRef]
15. Chen, H.; Liu, Y.; Yang, F.; Wei, M.; Zhao, X.; Ning, Y.; Liu, Q.; Zhang, Y.; Fu, Q.; Bao, X. Active Phase of FeO_x/Pt Catalysts in Low-Temperature CO Oxidation and Preferential Oxidation of CO Reaction. *J. Phys. Chem. C* **2017**, *121*, 10398–10405. [CrossRef]
16. Fukuoka, A.; Kimura, J.; Oshio, T.; Sakamoto, Y.; Ichikawa, M. Preferential Oxidation of Carbon Monoxide Catalyzed by Platinum Nanoparticles in Mesoporous Silica. *J. Am. Chem. Soc.* **2007**, *129*, 10120–10125. [CrossRef] [PubMed]
17. Luengnaruemitchai, A.; Srihamat, K.; Pojanavaraphan, C.; Wanchanthuek, R. Activity of Au/Fe_2O_3–TiO_2 catalyst for preferential CO oxidation. *Int. J. Hydrog. Energy* **2015**, *40*, 13443–13445. [CrossRef]
18. Ilieva, L.; Petrova, P.; Pantaleo, G.; Zanella, R.; Liotta, L.F.; Georgiev, V.; Boghosian, S.; Kaszkur, Z.; Sobczak, J.W.; Lisowski, W.; et al. Gold catalysts supported on Y-modified ceria for CO-free hydrogen production *via* PROX. *Appl. Catal. B. Environ.* **2016**, *188*, 154–168. [CrossRef]
19. Martínez-Arias, A.; Gamarra, D.; Hungría, A.B.; Fernández-García, M.; Munuera, G.; Hornés, A.; Bera, P.; Conesa, J.C.; Cámara, A.L. Characterization of Active Sites/Entities and Redox/Catalytic Correlations in Copper-Ceria-Based Catalysts for Preferential Oxidation of CO in H_2-Rich Streams. *Catalysts* **2013**, *3*, 378–400. [CrossRef]
20. Konsolakis, M. The role of Copper-Ceria interactions in catalysis science: Recent theoretical and experimental advances. *Appl. Catal. B. Environ.* **2016**, *198*, 49–66. [CrossRef]
21. Liu, X.; Lu, J.; Qian, K.; Huang, W.; Luo, M. A comparative study of formaldehyde and carbon monoxide complete oxidation on MnO_x–CeO_2catalyst. *J. Rare Earths* **2009**, *27*, 418–424. [CrossRef]
22. Delimaris, D.; Ioannides, T. VOC oxidation over MnO_x–CeO_2 catalysts prepared by a combustion method. *Appl. Catal. B Environ.* **2008**, *84*, 303–312. [CrossRef]
23. Xingyi, W.; Qian, K.; Dao, L. Catalytic combustion of chlorobenzene over MnOx–CeO_2 mixed oxide catalysts. *Appl. Catal. B Environ.* **2009**, *86*, 166–175. [CrossRef]
24. Wang, Z.; Shen, G.; Li, J.; Liu, H.; Wang, Q.; Chen, Y. Catalytic removal of benzene over CeO_2–MnO_x composite oxides prepared by hydrothermal method. *Appl. Catal. B Environ.* **2013**, *138*, 253–259. [CrossRef]
25. Mishra, A.; Prasad, R. A Review on Preferential Oxidation of Carbon Monoxide in Hydrogen Rich Gases. *Bull. Chem. React. Eng. Catal.* **2011**, *6*, 1–14. [CrossRef]
26. Liao, X.; Chu, W.; Dai, X.; Pitchon, V. Bimetallic Au–Cu supported on ceria for PROX reaction: Effects of Cu/Au atomic ratios and thermal pretreatments. *Appl. Catal. B Environ.* **2013**, *142–143*, 25–37. [CrossRef]
27. Trovarelli, A.; Fornasiero, P. *Catalysis by Ceria and Related Materials*, 2nd ed.; Graham, J.H., Ed.; Catalytic Science Series; Imperial College Press: London, UK, 2002.
28. Cecilia, J.A.; Arango-Díaz, A.; Franco, F.; Jiménez-Jiménez, J.; Storaro, L.; Moretti, E.; Rodríguez-Castellón, E. CuO-CeO_2 supported on montmorillonite-derived porous clay heterostructures (PCH) for preferential CO oxidation in H_2-rich stream. *Catal. Today* **2015**, *253*, 126–136. [CrossRef]
29. Kahlich, M.J.; Gasteiger, H.A.; Behm, R.J. Kinetics of the Selective Low-Temperature Oxidation of CO in H_2-Rich Gas over Au/α-Fe_2O_3. *J. Catal.* **1999**, *182*, 430–440. [CrossRef]
30. Schubert, M.M.; Kahlich, M.J.; Gasteiger, H.A.; Behm, R.J. Correlation between CO surface coverage and selectivity/kinetics for the preferential CO oxidation over Pt/γ-Al_2O_3 and Au/α-Fe_2O_3: An in-situ DRIFTS study. *J. Power Sources* **1999**, *84*, 175–182. [CrossRef]
31. Crisafulli, C.; Scirè, S.; Maggiore, R.; Minicò, S.; Galvagno, S. CO_2 reforming of methane over Ni–Ru and Ni–Pd bimetallic catalysts. *Catal. Lett.* **1999**, *59*, 21–26. [CrossRef]
32. Tang, X.; Zhang, B.; Li, Y.; Xu, Y.; Xin, Q.; Shen, W. Carbon monoxide oxidation over CuO/CeO_2 catalysts. *Catal. Today* **2004**, *93*, 191–198. [CrossRef]
33. Wang, L.; Chen, J.; Patel, A.; Rudolph, V.; Zhu, Z. Catalytic performance of Ru nanoparticles supported on different mesoporous silicas for preferential oxidation of CO in H_2-rich atmosphere. *Appl. Catal. A Gen.* **2012**, *447–448*, 200–209. [CrossRef]

34. Ilieva, L.; Pantaleo, G.; Ivanova, I.; Maximova, A.; Zanella, R.; Kaszkur, Z.; Venezia, A.M.; Andreeva, D. Preferential oxidation of CO in H_2 rich stream (PROX) over gold catalysts supported on doped ceria: Effect of preparation method and nature of dopant. *Catal. Today* **2010**, *158*, 44–55. [CrossRef]
35. Tu, Y.B.; Luo, J.Y.; Meng, M.; Wang, G.; He, J.J. Ultrasonic-assisted synthesis of highly active catalyst Au/MnO_x–CeO_2 used for the preferential oxidation of CO in H_2-rich stream. *Int. J. Hydrog. Energy* **2009**, *34*, 3743–3754. [CrossRef]
36. Stobe, E.R.; de Boer, B.A.; Geus, J.W. The reduction and oxidation behaviour of manganese oxides. *Catal. Today* **1999**, *47*, 161–167. [CrossRef]
37. Fiorenza, R.; Scirè, S.; Venezia, A.M. Carbon supported bimetallic Ru-Co catalysts for H_2 production through $NaBH_4$ and NH_3BH_3 hydrolysis. *Int. J. Energy Res.* **2018**, *42*, 1183–1195. [CrossRef]
38. Zhu, H.; Qin, Z.; Shan, W.; Shen, W.; Wang, J. Pd/CeO_2–TiO_2 catalyst for CO oxidation at low temperature: A TPR study with H_2 and CO as reducing agents. *J. Catal.* **2004**, *225*, 267–277. [CrossRef]
39. Jen, H.W.; Graham, G.W.; Chun, W.; McCabe, R.W.; Cuif, J.P.; Deutsch, S.E.; Touret, O. Characterization of model automotive exhaust catalysts: Pd on ceria and ceria–zirconia supports. *Catal. Today* **1999**, *50*, 309–328. [CrossRef]
40. Tabakova, T.; Boccuzzi, F.; Manzoli, M.; Sobczak, J.W.; Idakiev, V.; Andreeva, A. A comparative study of nanosized IB/ceria catalysts for low-temperature water-gas shift reaction. *Appl. Catal. A Gen.* **2006**, *298*, 127–143. [CrossRef]
41. Machida, M.; Uto, M.; Kurogi, D.; Kijima, T. MnO_x-CeO_2 Binary Oxides for Catalytic NOx Sorption at Low Temperatures. Sorptive Removal of NO_x. *Chem. Mater.* **2000**, *12*, 3158–3164. [CrossRef]
42. Dollimore, D.; Heal, G.R. An improved method for the calculation of pore size distribution from adsorption data. *J. Appl. Chem.* **1964**, *14*, 109–114. [CrossRef]
43. Scirè, S.; Riccobene, P.M.; Crisafulli, C. Ceria supported group IB metal catalysts for the combustion of volatile organic compounds and the preferential oxidation of CO. *Appl. Catal. B Environ.* **2010**, *101*, 109–117. [CrossRef]
44. Song, X.; Jiang, N.; Li, Y.; Xu, D.; Qiu, G. Synthesis and Characterization of Y-Doped Mesoporous CeO_2 Using A Chemical Precipitation Method. *J. Rare Earths* **2007**, *25*, 428–433.
45. Natile, M.M.; Boccaletti, G.; Glisenti, A. Properties and Reactivity of Nanostructured CeO_2 Powders: Comparison among Two Synthesis Procedures. *Chem. Mater.* **2005**, *17*, 6272–6286. [CrossRef]
46. Rosynek, M.P.; Magnuson, D.T. Infrared study of carbon dioxide adsorption on lanthanum sesquioxide and trihydroxide. *J. Catal.* **1977**, *48*, 417–421. [CrossRef]
47. Davydov, A. *Molecular Spectroscopy of Oxide Catalyst Surfaces*; Sheppard, N.T., Ed.; John Wiley & Sons Ltd.: Chichester, UK, 2003.
48. Li, C.; Sakata, Y.; Arai, T.; Domen, K.; Maruya, K.I.; Onishi, T. Carbon monoxide and carbon dioxide adsorption on cerium oxide studied by Fourier-transform infrared spectroscopy. Part 1.—Formation of carbonate species on dehydroxylated CeO_2, at room temperature. *J. Chem. Soc. Faraday Trans.* **1989**, *85*, 929–943. [CrossRef]
49. Vayssilov, G.N.; Mihaylov, M.; Petkov, P.S.; Hadjiivanov, K.I.; Neyman, K.M. Reassignment of the Vibrational Spectra of Carbonates, Formates, and Related Surface Species on Ceria: A Combined Density Functional and Infrared Spectroscopy Investigation. *J. Phys. Chem. C* **2011**, *115*, 23435–23454. [CrossRef]
50. Gulino, A.; Mineo, P.; Scamporrino, E.; Vitalini, D.; Fragalà, I. Spectroscopic and Microscopic Characterization and Behavior of an Optical pH Meter Based on a Functional Hybrid Monolayer Molecular System: Porphyrin Molecules Covalently Assembled on a Molecularly Engineered Silica Surface. *Chem. Mater.* **2006**, *18*, 2404–2410. [CrossRef]
51. Gulino, A.; Condorelli, G.G.; Mineo, P.; Fragalà, I. An x-ray photoelectron spectra and atomic force microscopy characterization of silica substrates engineered with a covalently assembled siloxane monolayer. *Nanotechnology* **2005**, *16*, 2170. [CrossRef] [PubMed]
52. Gulino, A.; Gupta, T.; Mineo, P.; van der Boom, M.E. Selective NO_x optical sensing with surface-confined osmium polypyridyl complexes. *Chem. Commun.* **2007**, *46*, 4878–4880. [CrossRef]
53. Zawadzki, M.; Okal, J. Synthesis and structure characterization of Ru nanoparticles stabilized by PVP or γ-Al_2O_3. *J. Mater. Res. Bull.* **2008**, *43*, 3111–3121. [CrossRef]
54. Gulino, A.; Egdell, R.G.; Fragalà, I. Low-temperature stabilisation of tetragonal zirconia by antimony. *J. Mater. Chem.* **1996**, *11*, 1805–1809. [CrossRef]

55. Motiei, L.; Lahav, M.; Gulino, A.; Iron, M.A.; van der Boom, M.E. Electrochemical Characteristics of a Self-Propagating Molecular-Based Assembly. *J. Phys. Chem. B* **2010**, *114*, 14283–14286. [CrossRef] [PubMed]
56. Folkesson, B. ESCA studies on the charge distribution in some dinitrogen complexes of rhenium, iridium, ruthenium, and osmium. *Acta Chem. Scand.* **1973**, *27*, 287–302. [CrossRef]
57. Biesinger, M.C.; Payne, B.P.; Grosvenor, A.P.; Lau, L.W.M.; Gerson, A.R.; Smart, R.S.C. Resolving surface chemical states in XPS analysis of first row transition metals, oxides and hydroxides: Cr, Mn, Fe, Co and Ni. *Appl. Surf. Sci.* **2011**, *257*, 2717–2730. [CrossRef]
58. Militello, M.C.; Simko, S.J. Elemental Palladium by XPS. *Surf. Sci. Spectra* **1994**, *3*, 387–394. [CrossRef]
59. Powell, C.J. Recommended Auger parameters for 42 elemental solids. *J. Electron. Spectrosc. Relat. Phenom.* **2012**, *185*, 1–3. [CrossRef]
60. Pulm, H.; Hohlneicher, G.; Freund, H.-J.J. Charge distribution in some ternary vintl phases as studied by v-ray photoelectron spectroscopy. *Less Common Met.* **1986**, *115*, 127–143. [CrossRef]
61. Ji, P.; Zhang, J.; Chen, F.; Anpo, M. Ordered Mesoporous CeO_2 Synthesized by Nanocasting from Cubic Ia3d Mesoporous MCM-48 Silica: Formation, Characterization and Photocatalytic Activity. *J. Phys. Chem. C* **2008**, *112*, 17809–17813. [CrossRef]
62. Gulino, A.; Dapporto, P.; Rossi, P.; Fragalà, I. Synthesis and Characterization of Liquid MOCVD Precursors for Thin Films of Cadmium Oxide. *Chem. Mater.* **2002**, *14*, 4955–4962.
63. Chen, H.; Sayari, A.; Adnot, A.; Larachi, F. Composition–activity effects of Mn–Ce–O composites on phenol catalytic wet oxidation. *Appl. Catal. B Environ.* **2001**, *32*, 195–204. [CrossRef]
64. Tang, X.; Li, Y.; Huang, X.; Xu, Y.; Zhu, H.; Wang, J.; Shen, W. MnO_x-CeO_2 mixed oxide catalysts for complete oxidation of formaldehyde: Effect of preparation method and calcination temperature. *Appl. Catal. B Environ.* **2006**, *62*, 265–273. [CrossRef]
65. Solsona, B.; Hutchigns, G.J.; García, T.; Taylor, S.H. Improvement of the catalytic performance of $CuMnO_x$ catalysts for CO oxidation by the addition of Au. *New J. Chem.* **2004**, *28*, 708–711. [CrossRef]
66. Jones, C.; Cole, K.J.; Taylor, S.H.; Crudace, M.J.; Hutchigns, G.J. Copper manganese oxide catalysts for ambient temperature carbon monoxide oxidation: Effect of calcination on activity. *J. Mol. Catal. A Chem.* **2009**, *305*, 121–124. [CrossRef]
67. Arena, F.; Trunfio, G.; Negro, J.; Fazio, B.; Spadaro, L. Basic Evidence of the Molecular Dispersion of $MnCeO_x$ Catalysts Synthesized via a Novel "Redox-Precipitation" Route. *Chem. Mater.* **2007**, *19*, 2269–2276. [CrossRef]
68. Laguna, O.H.; Centeno, M.A.; Arzamendi, G.; Gandía, L.M.; Romero-Sarria, F.; Odriozola, J.A. Iron-modified ceria and Au/ceria catalysts for Total and Preferential Oxidation of CO (TOX and PROX). *Catal. Today* **2010**, *157*, 155–159. [CrossRef]
69. Scirè, S.; Minicò, S.; Crisafulli, C.; Satriano, C.; Pistone, A. Catalytic combustion of volatile organic compounds on gold/cerium oxide catalysts. *Appl. Catal. B Environ.* **2003**, *40*, 43–49. [CrossRef]
70. Doornkamp, C.; Ponec, V. The universal character of the Mars and Van Krevelen mechanism. *J. Mol. Catal. A Chem.* **2000**, *162*, 19–32. [CrossRef]
71. Rosso, I.; Antonini, M.; Galletti, C.; Saracco, G.; Specchia, V. Selective CO-oxidation over Ru-based catalysts in H_2-rich gas for fuel cell applications. *Top. Catal.* **2004**, *30*, 475–480. [CrossRef]
72. Xu, J.; Xu, X.C.; Ouyang, L.; Yang, X.-Y.; Mao, W.; Su, J.; Han, Y.-F. Mechanistic study of preferential CO oxidation on a Pt/NaY zeolite catalyst. *J. Catal.* **2012**, *287*, 114–123. [CrossRef]
73. Chin, S.Y.; Alexeev, O.S.; Amiridis, M.D. Preferential oxidation of CO under excess H_2 conditions over Ru catalysts. *Appl. Catal. A Gen.* **2005**, *286*, 157–166. [CrossRef]
74. Barbato, P.S.; Colussi, S.; Di Benedetto, A.; Landi, G.; Lisi, L.; Llorca, J.; Trovarelli, A. CO preferential oxidation under H_2-rich streams on copper oxide supported on Fe promoted CeO_2. *Appl. Catal. A Gen.* **2015**, *506*, 268–277. [CrossRef]
75. Gao, Z.; Liu, Y.; He, Q.; Ma, H.; Li, Z.M. Preferential oxidation of CO and its subsequent methanation in H_2-rich gas over CuO-NiO/CeO_2 catalysts. *Int. J. Hydrog. Energy* **2016**, *41*, 4646–4659. [CrossRef]
76. Kim, Y.H.; Park, E.D.; Lee, H.C.; Lee, D. Selective CO removal in a H_2-rich stream over supported Ru catalysts for the polymer electrolyte membrane fuel cell (PEMFC). *Appl. Catal. A Gen.* **2009**, *366*, 363–369. [CrossRef]
77. Alayoglu, S.; Nilekar, A.U.; Mavrikakis, M.; Eichhorn, B. Ru–Pt core–shell nanoparticles for preferential oxidation of carbon monoxide in hydrogen. *Nat. Mater.* **2008**, *7*, 333–338. [CrossRef] [PubMed]

78. Pozdnyakova, O.; Teschner, D.; Wootsch, A.; Kröhnert, J.; Steinhauer, B.; Sauer, H.; Toth, L.; Jentoft, F.C.; Knop-Gericke, A.; Paál, Z.; et al. Preferential CO oxidation in hydrogen (PROX) on ceria-supported catalysts, part I: Oxidation state and surface species on Pt/CeO_2 under reaction conditions. *J. Catal.* **2006**, *237*, 1–16. [CrossRef]
79. Martínez, L.M.; Laguna, O.H.; López-Cartes, C.; Centeno, M.A. Synthesis and characterization of Rh/MnO_2-CeO_2/Al_2O_3 catalysts for CO-PrOx reaction. *Mol. Catal.* **2017**, *440*, 9–18. [CrossRef]
80. Zhao, Z.; Bao, T.; Li, Y.; Min, X.; Zhao, D.; Muhammad, T. The supported CeO_2/Co_3O_4–MnO_2/CeO_2 catalyst on activated carbon prepared by a successive-loading approach with superior catalytic activity and selectivity for CO preferential oxidation in H_2-rich stream. *Catal. Comm.* **2014**, *48*, 24–28. [CrossRef]
81. Chang, L.H.; Sasirekha, N.; Chen, Y.W.; Wang, W.J. Preferential Oxidation of CO in H_2 Stream over Au/MnO_2-CeO_2 Catalysts. *Ind. Eng. Chem. Res.* **2006**, *45*, 4927–4935. [CrossRef]
82. Cecilia, J.A.; Arango-Diaz, A.; Marrero-Jerez, J.; Nunez, P.; Moretti, E.; Storaro, L.; Rodiguez-Castellon, E. Catalytic Behaviour of CuO-CeO_2 Systems Prepared by Different Synthetic Methodologies in the CO-PROX Reaction under CO_2-H_2O Feed Stream. *Catalysts* **2017**, *7*, 160. [CrossRef]
83. Briggs, D.; Grant, J.T. *Surface Analysis by Auger and X-Ray Photoelectron Spectroscopy*; IM Publications: Chichester, UK; Surface Spectra Ltd.: Manchester, UK, 2003.
84. Gulino, A. Structural and electronic characterization of self-assembled molecular nanoarchitectures by X-ray photoelectron spectroscopy. *Anal. Bioanal. Chem.* **2013**, *405*, 1479–1495. [CrossRef] [PubMed]